Research Square

Preprints are preliminary reports that have not undergone peer review.
They should not be considered conclusive, used to inform clinical practice,
or referenced by the media as validated information.

# Spin-induced polarization enables anodic carbon–nitrogen coupling electrocatalysis for sustainable formamide synthesis

**Ben Liu**

ben.liu@scu.edu.cn

Sichuan University https://orcid.org/0000-0003-1305-5900

**Shu Han**

Sichuan University

**Deqing Tang**

Sichuan University

**Rui Ding**

Sichuan University

**Article**

**Keywords:**

**Posted Date:** November 6th, 2026

**DOI:** https://doi.org/10.21203/rs.3.rs-11503736/v1

**License:** This work is licensed under a Creative Commons Attribution 4.0 International License.
Read Full License

**Additional Declarations:** There is **NO** Competing Interest.

# Spin-induced polarization enables anodic carbon–nitrogen coupling electrocatalysis for sustainable formamide synthesis

Shu Han, Deqing Tang, Rui Ding, and Ben Liu*

Key Laboratory of Green Chemistry and Technology of Ministry of Education, National and Local Joint Engineering Laboratory of Energy Plant Bio-fuel Preparation and Utilization, College of Chemistry, Sichuan University, Chengdu 610064, China. *E-mail: ben.liu@scu.edu.cn

**Abstract**

Organic electrosynthesis driven by the renewable electricity and reacted in water offers a green route to prepare higher value-added formamide by constructing carbon–nitrogen (C–N) coupling reactions. Currently, electrochemical formamide synthesis focuses mainly on cathodic processes, required relatively expensive substrates and high electricity and equipment costs, which greatly hinders practical application in industry. Herein, we reported anodic electrosynthesis of formamide from mixed polyols and ammonia by a spin-induced polarization strategy. We proposed that alloying Fe sites into mesoporous CuO broke its long-range antiferromagnetic order and created spin-polarized surface with localized paramagnetic centers. Spin-induced polarization strategy promoted the formation and stabilization of $*NH_2$ intermediates without overoxidation to unreacted $NO_3^-$, which behaved as the dominant nucleophile to mediate concerted C–C cleavage and C–N coupling reactions for selective formamide synthesis with minor byproducts at anode. In a flow cell, it delivered a superior formamide Faradaic efficiency of 70.4% and selectivity of 99.0%, with the high net profit of US$1,598 per ton. Meanwhile, the strategy has generally been applied to mixed polyols substrates mimicking the real feedstock from renewable biomass, which further underscored promising industrial application potential. This work establishes a new paradigm to construct efficient C–N coupling reactions for various value-added amides by a spin-state engineering strategy.

**Main**

Formamide, as a high-value-added chemical, is widely utilized in the synthesis of pharmaceuticals, fragrances, dyes, and fine chemicals. It has a market price of approximately USD 3,000 per ton, accompanied by the continuously growing market demand[1-5]. Electrocatalytic technology driven by the renewable electricity has recently offered an important route to achieve amide synthesis by constructing carbon–nitrogen (C–N) bonds from small carbon-containing molecules ($CO_2$, CO, HCHO, $CH_3OH$, etc) and nitrogen-containing molecules

($NO_3^-$, $NO_2^-$, $NO_x$, $N_2$, $NH_3$, etc), which also reduces fossil energy dependence and enables green nitrogenous chemical production[6-10]. Currently, electrochemical formamide synthesis focuses mainly on cathodic processes, using $CO_2$ as the carbon source and $NO_3^-$/$NO_2^-$ as the nitrogen source (**Fig 1a**)[11-14]. However, such pathways involve multielectron transfer routes, and require relatively expensive substrates and high electricity and equipment costs, which result in a remarkably high production cost of formamide (**Fig 1b**)[15,16]. Alternatively, anodic processes utilize the electrooxidation of alcohol molecules and ammonia to achieve C–N coupling reactions, feature fewer electron transfers and mild reaction conditions as well as renewable substrates, which thus offers better economic viability for formamide synthesis (**Fig 1c**)[17-20]. However, the substrate of existing anodic reactions exclusively restricted to relatively expensive and toxic methanol, limiting its further practical application in the future[21,22]. Polyols, as important platform molecules derived from waste biomass, are abundant, renewable, and low in toxicity[23-25]. We thus expect that polyols can undergo selective oxidation electrocatalysis to generate electrophilic aldehyde/carbonyl intermediates *in situ*, which subsequently proceed C–N coupling reactions with nitrogen-containing nucleophiles, proposing an industrially promising route for anodic formamide synthesis.

In principle, polyols represented by ethylene glycol involve C–C bond oxidation cleavage during electrocatalytic formamide synthesis at anode. Traditional strategies mainly rely on *OH radical attack to achieve bond cleavage (**Fig 1d**)[3,26-28]. Competitively, a high flux of *OH not only promotes bond cleavage but also readily overoxidizes key aldehyde intermediates to undesirable formate[29,30]. More critically, existing strategies involves the activation of carbon-based intermediates while neglecting the effective protection of nitrogen intermediates (*$NH_2$)[31-33]. Although the long-range antiferromagnetic CuO catalysts exhibit high activity and selectivity in regulating selective oxidation of carbon substrates, their intrinsic antiparallel spin structure constitutes an inherent limitation for highly selective conversion of nitrogen species[26,34-36]. Adjacent antiparallel spin environment readily induces nonproductive coupling between doublet-state *$NH_2$ and *OH, leading to deep oxidation of nitrogen species to unreacted $NO_3^-$[37]. This not only causes severe nitrogen loss and substantial wasted electron consumption, markedly lowering the Faradaic efficiency (FE), but also sharply reduces the steady-state concentration of surface *$NH_2$, preventing it from effectively intercepting the carbon intermediates generated by C–C bond cleavage. Such failure of nitrogen-side protection, in turn, erodes original carbon-side control advantage of CuO, as aldehyde intermediates that are not promptly C–N coupling become available for deep carboxylation as the side reactions. Therefore, it is highly desirable to precisely regulate the surface spin state of CuO to stabilize *$NH_2$ and block its detrimental coupling with *OH that breaks the selectivity bottleneck in anodic formamide electrosynthesis and thus drives the strategy across the breakeven point toward economic profitability (**Fig 1e**).

Herein, we proposed, for the first time, a spin-induced polarization regulation strategy to break the long-range antiferromagnetic order of CuO and enabled the localized paramagnetic centers to solve the selectivity bottleneck for anodic formamide electrosynthesis. By alloying Fe sites, a spin-polarized mesoporous (CuFe)O (meso-(CuFe)O) stabilized $*NH_2$ through an exchange field without the coupling with *OH by the spin forbiddenness, thereby mitigating the overoxidation of $NH_3$ to $NO_3^-$. Sufficiently accumulated $*NH_2$ timely reacted with glycolaldehyde generated from ethylene glycol oxidation, undergoing $*NH_2$-mediated C–N coupling accompanied by C–C bond cleavage to generate formamide with recordable selectivity. This $*NH_2$-mediated pathway achieved superior formamide FE of above 60% within the reaction potentials of 2.0–2.4 V [versus reversible hydrogen electrode (vs. RHE) hereafter] in a flow cell. After continuous operation for 20 h, the FE remained at 60%, with the proportion of formamide among $C_1$ products of greater than 99%. More impressively, it has also been extended to polyols systems, including methanol, glycerol, erythritol, xylitol, sorbitol, and their mixed polyols, which thus enabled further potential application in industry. This spin-polarization regulation strategy not only provided a new paradigm for designing efficient C–N coupling electrocatalysts through the spin engineering, but also, with the $*NH_2$-mediated pathway at its core, injected strong momentum into the value-added upgrading of biomass resources and the sustainable electrocatalytic synthesis of high-value-added chemicals.

## Results and discussion

### Electrocatalysts characterizations

Meso-(CuFe)O nanosheets rich in penetrating mesopores and possessing binary metal oxide compositions were designed for further utilization since they enabled abundant highly active site and good mass transport ability. Low-magnification transmission electron microscopy (TEM) and high-angle annular dark-field scanning TEM (HAADF-STEM) images revealed a uniform sheet-like morphology (**Fig 2a and S1**). There were numerous highly dispersed mesopores distributed throughout the nanosheets, with the sizes ranging from 4.0 to 10 nm and pronounced penetrating characteristics. High-magnification and corresponding high-resolution TEM images further revealed penetrated mesopores surrounded by highly crystalline wall with clear lattice fringes having a *d*-spacing distance of 0.254 nm that corresponded to the (111) plane in the C2/c space group (**Fig 2b**). The lattice fringes extended continuously around mesoporous channels, indicating that abundant high-energy facets were exposed at mesopore edges, which favored the adsorption and activation of reactant molecules for electrocatalysis[38-40]. Energy-dispersive X-ray spectroscopy (EDS) elemental mapping images showed spatially uniform distributions of Cu, Fe, and O within the mesoporous nanosheets, without

obvious elemental segregation (**Fig 2c**). The Cu/Fe atomic ratio was determined to be 1:9, and the O content was 48.3 at% (**Table S1**). X-ray diffraction (XRD) patterns further indicated that the nanosheets possessed a crystal structure similar to that of monometallic CuO, confirming that Fe alloying did not alter the crystal structure of the host CuO (**Fig S2 and S3**).

Magnetic properties of meso-(CuFe)O were investigated by the temperature-dependent magnetic susceptibility measurements and compared with monometallic meso-CuO counterpart. For pristine meso-CuO, the inverse magnetic susceptibility (1/χ) gradually decreased with increasing temperatures, exhibiting typical antiferromagnetic characteristics (**Fig 2d**). That was, the antiparallel alignment of adjacent $Cu^{2+}$ magnetic moments led to mutual cancellation of the net magnetic moments (**Fig S4**)[41,42]. After Fe being alloyed, the long-range antiferromagnetic order was disrupted, the magnetic response of meso-(CuFe)O was markedly enhanced, in which the M–T curves exhibited paramagnetic characteristics over the tested temperature range (**Fig 2e and S5**)[43]. As the Fe alloyed amounts increased from 10% to 20%, the effective magnetic moment increased only slightly from 0.965 to 1.044 $\mu_{eff}$ (**Fig S6**). The increase was far smaller than expected from a doubling of the Fe content, indicating that Fe did not act as the isolated paramagnetic centers and that some magnetic moments were cancelled by antiferromagnetic coupling and spin compensation[44,45]. Projected density of states (PDOS) analysis by the density functional theory (DFT) calculations indicated that the spin-up and spin-down projections of the total Cu 3*d* states in pristine CuO were essentially coincident, reflecting antiferromagnetic compensation (**Fig 2f**). For meso-(CuFe)O, differently, the total Cu 3*d* states were no longer fully degenerated, and weak spin polarization emerged, with the spin-up and spin-down *d*-band centers located at −3.26 and −3.22 eV, respectively. This indicated that alloying a small amount of Fe effectively perturbed the original antiferromagnetic compensation environment of CuO, inducing a tendency toward the net spin polarization in the Cu 3*d* states. Therefore, the alloying of Fe not only provided isolated paramagnetic centers, but also modulated the spin structure of CuO through Cu–O–Fe hybridization/superexchange, generating finite yet discernible Cu 3*d* spin polarization at low doping amounts (**Fig 2g**)[46].

**Performance evaluation**

Anodic electrocatalytic performance for formamide synthesis over spin-polarized meso-(CuFe)O was evaluated in an electrolyte of 0.30 M $(NH_4)_2SO_4$ containing 4.0 M ethylene glycol (carbon source) and 0.35 M $NH_3$ (nitrogen source). Linear sweep voltammetry (LSV) curves showed, at the same current density of 5.0 mA $cm^{-2}$, meso-(CuFe)O required only 1.81 V, which was 250 and 210 mV lower than those under OER

conditions (2.06 V) and in the ethylene glycol-only system (2.02 V), indicating high performance for ethylene glycol and $NH_3$ oxidation electrocatalysis (**Fig S7**). The $^1H$ nuclear magnetic resonance ($^1H$ NMR) spectroscopy was further performed for product analysis. Impressively, ethylene glycol was predominantly converted to formamide, with negligible formate formation (**Fig 3a**). During deep electrocatalysis at 2.1 V (with the charge passed reaching 800 C), the FE for formamide gradually decreased from 54.3% to 39.0%, indicating that meso-(CuFe)O sustained continuous formamide synthesis during prolonged electrocatalysis (**Fig 3b**). This decrease in FE was likely attributable to continuous consumption of $NH_3$, which led to an insufficient supply of $*NH_2$ intermediates and thereby reduced the contribution of formamide formation. The formamide electrosynthesis performance was further examined over a wide potential window of 2.0–2.6 V (**Fig 3c**). The FE reached its maximum of 62.8% at 2.0 V and remained above 50% throughout the tested potentials. As the potential increased, the current density increased, and the formamide yield rate gradually rose, reaching a maximum of 0.41 mmol $cm^{-2}$ $h^{-1}$ at 2.6 V. When the potential was increased to 2.3 V, formate began to be detected above the detection limit, suggesting that, at higher potentials, excess *OH may enhance side reaction of formaldehyde overoxidation (**Fig 3d**). Nevertheless, formamide still retained relatively high selectivity. By contrast, although meso-CuO also produced formamide, its highest FE was only 46.3%, with FE values being markedly lower than those of meso-(CuFe)O at all tested potentials (**Fig S8**).

A series of meso-(CuFe)O catalysts with different Fe alloyed amounts were evaluated under same conditions for anodic formamide electrosynthesis (**Fig 3e and S9-12**). In the absence of Fe alloy, the FE for formamide was 46.3%. Upon 5% Fe being alloyed, the FE increased sharply to 61.5%, indicating that even a small amount of Fe substantially suppressed competing side reactions (**Fig S13a**). Upon further increasing the Fe alloy to 15%, the FE reached a maximum of approximately 67.6% (**Fig S13b**); however, the formamide formation rate decreased to 0.20 mmol $cm^{-2}$ $h^{-1}$. At an Fe alloy of 20%, both the FE and the formation rate declined (**Fig S13c**). These results demonstrated that Fe alloys exerted the contrasting effects on selectivity and formation rate for formamide synthesis: the highest formation rate occurred at a relatively low Fe alloyed amount, whereas optimal selectivity was achieved at a slightly higher Fe alloyed amount. Electrocatalytic cycling stability was further assessed for formamide electrosynthesis at anode. After 10 consecutive cycles being conducted at 2.1 V, both formamide FE and yield rate remained relatively stable, with no appreciable decay, indicating sustainable performance of meso-(CuFe)O for formamide electrosynthesis (**Fig 3f**).

Since alcohols, especially derived from waste biomass, are mixed polyols, we thus studied electrocatalytic performance of spin-polarized meso-(CuFe)O for anodic formamide synthesis with a series of polyols as carbon substrates (**Fig 3g**). Here, five other biomass-derived alcohols, including methanol, glycerol, erythritol,

xylitol, and sorbitol, were evaluated under same conditions (**Fig 3h and Table S2**). Impressively, all five alcohol substrates enabled high FE and yield rates for formamide electrosynthesis. With increasing carbon chain lengths, the FE first increased and then decreased slightly, reaching a maximum of 79.3% with erythritol as the substrate. More importantly, there were no other carbon products during the electrocatalysis. It indicated good substrate generality for formamide synthesis toward diverse $C_1$–$C_6$ alcohol platform molecules (**Fig S14**). Furthermore, an equimolar mixture of six ($C_1$–$C_6$) alcohols (1:1:1:1:1:1) was employed to evaluate electrocatalytic performance in a mixed polyol system (**Fig 3i**). Within the potential window of 2.0–2.4 V, the formamide yield rate increased progressively with increasing the potentials, whereas the formate formation rate remained extremely low (<0.03 mmol $cm^{-2}$ $h^{-1}$) (**Fig S15**). These results clearly demonstrated that anodic formamide electrosynthesis over spin-polarized meso-(CuFe)O was applicable not only to single alcohol substrates but also to mixed systems, which thus validated its substrate generality and practical application potential in industry.

**Electrocatalytic pathway**

To elucidate how spin-polarized meso-(CuFe)O promoted anodic formamide synthesis from ethylene glycol and $NH_3$, *in situ* electrochemical Fourier transform infrared (FTIR) spectroscopy was employed to monitor the reaction intermediates and further reveal corresponding electrocatalytic pathway. In the presence of ethylene glycol only, a series of characteristic peaks gradually emerged as electrocatalysis proceeded, including those at 1677 $cm^{-1}$ (formaldehyde C=O), 1526 $cm^{-1}$ (carboxylate $COO^-$ asymmetric stretching), 1356 $cm^{-1}$ (formate-related $COO^-$ vibration), 1289 $cm^{-1}$ (O–C–O), 1233 $cm^{-1}$ (C–O), 1174 $cm^{-1}$ (C–C), and 1089 $cm^{-1}$ (C–OH) (**Fig 4a**)[17,47,48]. It indicated that ethylene glycol underwent anodic C–C bond cleavage and deep oxidation to generate intermediates such as formaldehyde and formate. This was consistent with conventional *OH attack-mediated bond cleavage mechanism for polyol oxidation electrocatalysis. Upon the addition of $NH_3$, the signals changed markedly under same test conditions. In addition to retaining the formaldehyde signal at 1677 $cm^{-1}$ and the C–OH signal at 1089 $cm^{-1}$, a new C–N bond signal appeared at 1464 $cm^{-1}$, together with $NH_2$ vibrational peaks at 1268 and 1156 $cm^{-1}$, indicating that the overoxidation of both ethylene glycol and $NH_3$ was extremely weak (**Fig 4b**)[6,11,49,50]. Compared with the $NH_3$-free condition, the signals of deep oxidation products were markedly attenuated and even became undetectable after $NH_3$ was injected, whereas the signals of C–N coupling and $NH_2$-related products rapidly intensified[51]. It highlighted that the introduction of $NH_3$ into ethylene glycol altered electrocatalytic oxidation pathway and products. If $*NH_2$ acted merely as a downstream C–N coupling reagent, the product distribution from ethylene glycol bond cleavage should not change fundamentally. We thus deduced that $*NH_2$ may promote

C–C bond cleavage and drive the reaction for formamide synthesis by attacking the α-C of ethylene glycol or capturing the glycolaldehyde intermediate, thereby suppressing *OH-mediated overoxidation pathway.

DFT calculations were further performed to validate the $*NH_2$-mediated oxidation pathway for anodic formamide synthesis (**Table S3**). In the absence of $NH_3$, direct C–C bond cleavage of ethylene glycol by *OH to formaldehyde required a high energy barrier of 3.14 eV, indicating that *OH-dominated direct bond cleavage was kinetically unfavorable (**Fig 4c**). Upon the injection of $NH_3$, the reaction pathway was altered: ethylene glycol was first oxidized to glycolaldehyde through a step with a remarkably low energy barrier of 0.50 eV; subsequently, $*NH_2$ nucleophilically attacked glycolaldehyde, triggering C–N coupling reaction accompanied by C–C bond cleavage to generate one molecule of formamide and one molecule of formaldehyde. The newly generated formaldehyde further reacted with $*NH_2$ to complete the synthesis of a second formamide molecule. Compared with the high-barrier direct cleavage pathway in the absence of $NH_3$, it exhibited a markedly lower energy barrier in the rate-determining step and thus rendered the overall reaction feasible. The results theoretically demonstrated that $*NH_2$ did not merely serve as a nitrogen source for subsequent C–N coupling reaction but directly participate in the C–C bond cleavage and C–N coupling steps of glycolaldehyde, thereby kinetically suppressing *OH-mediated overoxidation for undesirable side reactions.

Proposed reaction pathway was then revealed by the tert-butanol trapping and Fenton experiments to exclude the role of *OH for anodic formamide synthesis. At 2.4 V, the addition of tert-butanol did not suppress formamide formation, whereas formate remained below the detection limit, indicating the independence of *OH in formamide synthesis (**Fig 4d**)[52]. Differently, introducing additional *OH *via* $Fe^{2+}$-mediated Fenton reaction promoted formate production and inhibited formamide synthesis (**Fig S16 and S17**). At a fixed $Fe^{2+}$ concentration, meanwhile, increasing the potential from 2.2 to 2.4 V markedly increased the formamide proportion among $C_1$ products (**Fig 4e**)[53]. Higher potentials enhanced electrocatalytic $*NH_2$ generation and facilitated $*NH_2$-mediated oxidation and C–N coupling pathway, making it more competitive against *OH-mediated deep oxidation for formate synthesis. These results indicated that $*NH_2$-mediated C–N coupling pathway was dominant for formamide synthesis, whereas *OH-mediated oxidation pathway favored ethylene glycol conversion to formate. Kinetically, apparent activation energy ($E_{app}$) values were measured at different applied potentials (**Fig 4f**)[54]. In the $NH_3$-free system, $E_{app}$ values increased from 13.5 to 18.5 kJ $mol^{-1}$ with increasing potentials, suggesting that the rate-determining barrier for ethylene glycol cleavage increased and that *OH-mediated C–C cleavage became kinetically less favorable. In the presence of ethylene glycol and $NH_3$, $E_{app}$ values were generally lower and less potential-dependent. At ≥2.0 V, it was

markedly lower than that of the $NH_3$-free system, indicating that *$NH_2$-mediated cleavage pathway was kinetically more favorable. The lower and more stable $E_{app}$ values demonstrated that *$NH_2$-mediated C–N coupling pathway was kinetically advantaged over *OH-mediated bond cleavage pathway.

On the basis of above results, we proposed an $NH_2$-mediated pathway involving the oxidative C–C bond cleavage of ethylene glycol coupled with the C–N coupling reaction for formamide synthesis (**Fig 4g**). Typically, ethylene glycol was first dehydrogenated electrocatalytically to glycolaldehyde, while $NH_3$ was dehydrogenated to generate nucleophilic *$NH_2$. *$NH_2$ attacked the carbon center of glycolaldehyde, promoting C–C bond cleavage and C–N coupling reaction to produce one molecule of formamide and one molecule of formaldehyde; the latter further reacted with nucleophilic *$NH_2$ to yield a second molecule of formamide. In this pathway, *$NH_2$ directly participated in C–C bond cleavage and was kinetically favored over direct *OH-mediated oxidation pathway, thereby effectively preventing the overoxidation of aldehyde intermediates to formate.

**Electrocatalytic mechanism**

The reason of why spin-polarized meso-(CuFe)O performed perfectly for selective formamide synthesis was then unveiled. *In situ* Bode plots were performed to reveal interfacial kinetics during electrocatalysis (**Fig S18**). In the ethylene glycol-only electrolyte, compared with meso-CuO, the phase angle peak of meso-(CuFe)O was located in a higher-frequency region, indicating faster kinetics for surface ethylene glycol dehydrogenation process (**Fig 5a**)[55,56]. After $NH_3$ addition, the phase angle peaks of two catalysts shifted to lower frequencies, with more pronounced peaks for meso-(CuFe)O, indicating that *$NH_2$ generation and *$NH_2$-mediated C–N coupling steps became more dominant (**Fig 5b**). Nitrogen species conversion experiments further confirmed favorable formation of *$NH_2$ and the inhibition of overoxidated $NO_3^-$ (**Fig S19 and S20**). For meso-CuO, the main overoxidation product of $NH_3$ was $NO_3^-$, with an FE as high as 43.5%. After 5% Fe being alloyed, the $NO_3^-$ FE rapidly decreased to 21.5%, reached a minimum of approximately 16.6% at 15% Fe, and slightly rebounded at 20% Fe (**Fig 5c**). Meanwhile, $E_{app}$ value for $NH_3$ overoxidation pathway to $NO_3^-$ increased to 18.1 kJ $mol^{-1}$ on meso-(CuFe)O, higher than that of 13.6 kJ $mol^{-1}$ on meso-CuO (**Fig 5d**). It further highlighted that the overoxidation route became kinetically more difficult after Fe was alloyed meso-CuO. We proposed that this suppression related to the spin forbiddenness induced by the spin-polarized surface of meso-(CuFe)O[57]. If *$NH_2$ and *OH adsorbed with the same spin orientation, their coupling from a triplet state to singlet $NH_2$–OH would require overcoming spin flip, thereby blocking the $NH_3$ overoxidation pathway to $NO_3^-$. Apparent activation energy measurements at multiple potentials further showed that, in

the range of 1.8–2.1 V, the overall $E_{app}$ values of $*NH_2$ generation and C–N coupling step on meso-(CuFe)O were markedly lower than those on meso-CuO (**Fig S21**). At above 2.2 V, the two values approached each other, indicating that the promotional effect of spin polarization on the $*NH_2$-mediated pathway remained effective over a relatively wide potential window. Similarly, *In situ* FTIR spectra indicated that, on meso-CuO without Fe alloys, $NH_3$ dehydrogenation to $*NH_2$ and subsequent C–N coupling reactions were relatively unfavorable, and a larger fraction of aldehyde intermediates were diverted to the overoxidation pathway (**Fig S22**). These results clearly confirmed that spin-polarized meso-(CuFe)O effectively suppressed $NH_3$ overoxidation and favored $*NH_2$-mediated C–N coupling reaction.

Electrocatalytic mechanism for anodic formamide synthesis was also revealed by spin-polarized DFT calculations (**Table S4**). $NH_3$ initially adsorbed on the catalyst surface as adsorbed $NH_3$, which subsequently dehydrogenated to generate the key intermediate of $*NH_2$. Compared with meso-CuO, the free energy of $*NH_2$ intermediate relative to $NH_3$ on spin-polarized meso-(CuFe)O decreased from −0.1 to −0.4 eV, indicating that the spin-polarized surface was more favorable for $NH_3$ dehydrogenation and $*NH_2$ stabilization (**Fig 5e**). The electronic-structure origin lay in the asymmetric spin-up and spin-down electronic states near the Fermi level of the spin-polarized surface, which provided electronic states with spins matching the unpaired electron of $*NH_2$, thereby lowering the energy of the $*NH_2$ intermediate through exchange interactions, promoting its generation, and increasing its surface coverage. Further comparison of the full free-energy evolution of ethylene glycol oxidation and C–N coupling reactions revealed that the free-energy increase for ethylene glycol dehydrogenation to glycolaldehyde decreased from 0.65 eV on meso-CuO to 0.50 eV on meso-(CuFe)O (**Fig 5f**). More critically, for the subsequent step in which $*NH_2$ attacked glycolaldehyde to induce C–N coupling accompanied by C–C bond cleavage, the free-energy change shifted from +0.22 eV (endothermic) on meso-CuO to −0.04 eV (exothermic) on spin-polarized meso-(CuFe)O, transforming from thermodynamically unfavorable to favorable. In this step, the unpaired electron of $*NH_2$ underwent ferromagnetic exchange coupling with the localized spins of the spin-polarized surface, forming a spin-parallel high-spin transition state. This lowered the transition-state energy through exchange interactions and promoted effective overlap between the N lone pair and the C=O $\pi^*$ antibonding orbital, enabling concerted C–N bond formation and C–C bond cleavage and thereby markedly reducing the rate-determining step barrier for formamide synthesis.

On the basis of above results and discussion, we reasonably proposed an electrocatalytic mechanism of spin-polarized meso-(CuFe)O for anodic formamide synthesis from ethylene glycol and $NH_3$ (**Fig 5g**). After Fe sites were alloyed into meso-CuO, the long-range antiferromagnetic order was disrupted, and spin-polarized sites

with localized net spin density were formed on the surface. This spin-polarized surface of meso-(CuFe)O promoted $NH_3$ dehydrogenation and stabilized $*NH_2$ intermediate through an exchange field; at the same time, the spin-polarized surface suppressed the coupling between $*NH_2$ and *OH through spin forbiddenness, thereby disfavoring the *OH-mediated overoxidation of aldehydes to formate and the overoxidation of $NH_3$ to $NO_3^-$. These two effects enabled the continuous accumulation and enrichment of $*NH_2$ on the surface, providing sufficient nitrogen-active species for the $*NH_2$-mediated pathway. Sufficient $*NH_2$ timely attacked glycolaldehyde generated from ethylene glycol oxidation, undergoing $*NH_2$-mediated C–N coupling reaction accompanied by C–C bond cleavage to produce one molecule of formamide and one molecule of formaldehyde; the newly generated formaldehyde was further captured by $*NH_2$ to complete the synthesis of a second molecule of formamide. This mechanism achieved synergistic regulation from the spin perspective, namely enriching $*NH_2$, enabling timely coupling, and suppressing overoxidation, highlighted the dominant role of the $*NH_2$-mediated pathway in anodic formamide synthesis. Meanwhile, it explained the significantly improved formamide selectivity after Fe being alloyed and provided a new strategy for designing efficient C–N coupling electrocatalysts through the spin engineering strategy.

**Large-scale electrosynthesis in a flow cell**

To further verify the feasibility of this strategy under practical conditions, formamide electrosynthesis of spin-polarized meso-(CuFe)O was evaluated in a flow cell. Over the potential range of 2.0–2.4 V, the formamide FE remained above 60%, reaching a maximum of 70.4% at 2.0 V, indicating that it retained high selectivity in the flow system (**Fig 6a**). During continuous operation at 2.2 V for 70 h, the current density exhibited no appreciable decay, the final FE remained at 59.7%. More impressively, the proportion of formamide among $C_1$ products remained consistently greater than 99%, demonstrating that good stability for the long-term operation (**Fig 6b**). Product analysis further showed that formamide was the predominant product after electrocatalysis, with only a very small amount of formic acid detected as a byproduct with formamide accounted for 99.6% of the detected carbon-containing products (**Fig 6c**). In deep-conversion experiments, when ethylene glycol conversion reached 31.1%, the formamide selectivity remained as high as 99.0%, whereas the selectivity for the overoxidation product of formic acid was only 0.76% (**Fig 6d and S23**). The results definitely highlighted high practical potential of the strategy in a flow cell for selective electrosynthesis of high value-added formamide at anode.

Techno-economic analysis was finally carried out to validate the economic superiority of this strategy for formamide synthesis (**Table S5**). Regarding production costs, anodic oxidation route circumvented the high

substrate prices and multi-electron energy penalties inherent to conventional cathodic pathways. By utilizing low-cost ethylene glycol and achieving high selectivity to prevent waste, the total production cost was significantly reduced to US$1,655 per ton. On the revenue side, the profitability was directly governed by the FE values. Driven by the spin-regulated strategy, the significantly enhanced FE values yielded a high net profit of US$1,598 (**Fig 6e**). This confirmed that the high FE successfully shifted the system well into the profitable region, safely surpassing the break-even threshold (**Fig S24**). Further analysis revealed that the process remained profitable over broad fluctuations in electricity price and formamide market price, indicating a certain degree of risk resistance (**Fig 6f**). Collectively, these results not only demonstrated that the strategy exhibited good stability and high selectivity in a flow cell but also translated the theoretical cost advantages of the anodic route into tangible economic benefits, providing a practical basis for designing efficient C–N coupling electrocatalysts through spin engineering.

**Conclusion and outlook**

In conclusion, we developed a new electrocatalytic route by the spin-induced polarization regulation strategy, in which Fe sites were alloyed into the CuO lattice to construct spin-polarized meso-(CuFe)O with localized paramagnetic centers, enabling highly selective electrosynthesis of formamide from biomass-derived polyols and $NH_3$ at anode. The spin-polarized surface stabilized *$NH_2$, promoted *$NH_2$-mediated C–C bond cleavage and C–N coupling reaction, and suppressed *OH-mediated overoxidation through spin forbiddenness, thereby simultaneously achieving high selectivity for both nitrogen and carbon products. In a flow cell, the FE of formamide remained above 60% over a potential window of 2.0–2.4 V, reaching a maximum of 70.4%. In the deep-conversion experiments, when ethylene glycol conversion reached 31.1%, the formamide selectivity remained as high as 99.04%, whereas the formate selectivity was only 0.76%. More importantly, this strategy was generally extendable to methanol, glycerol, erythritol, xylitol, sorbitol, and their mixed polyol systems, with high formamide selectivity. Techno-economic analysis indicated that this process achieved US$3,253 in revenue and US$1,656 in expenditure per ton of formamide produced, with a positive net profit and a certain degree of resistance to fluctuations in electricity price and market price.

This study, for the first time, applied an antiferromagnetic-to-local-paramagnetic spin transition to drive anodic electrocatalytic C–N coupling reactions for high value-added amides. More broadly, this work establishes a mechanistic paradigm in which electronic modulation serves not merely to tune activity but also to protect key nitrogen intermediates and steer the reaction away from the overoxidation. Looking ahead, we envision extending this principle beyond formamide synthesis to other C–N coupling reactions

and to the conversion of diverse biomass-derived platform molecules, where selective stabilization of reactive heteroatom intermediates is equally critical. Such efforts, together with the flow-cell engineering and techno-economic assessment, may accelerate the translation of this strategy toward scalable and economically viable electrosynthesis of high value-added nitrogen-containing chemicals from renewable biomass. We believe that this strategy establishes a promising design principle for efficient C–N coupling electrocatalysts and for the value-added upgrading of biomass resources.

**Methods**

For a full description of synthetic and theoretical methods, see the Supplementary Information.

**General procedure for synthesis of meso-(CuFe)O**

In a typical synthesis of meso-(CuFe)O nanosheets with 10% of Fe amount, tetraethylene glycol (30 mL) and deionized water (30 mL) were first mixed to form a homogeneous solution. Then, 0.60 g of urea, 0.50 mmol of $Fe(NO_3)_3{\cdot}9H_2O$, and 4.50 mmol of $Cu(NO_3)_2{\cdot}3H_2O$ were then added under continuous stirring for 1 h until complete dissolution. The resulting solution was transferred into a Teflon-lined stainless-steel autoclave, sealed, and reacted at 120 $^oC$ for 12 h for the hydrothermal reaction. After being cooled naturally to room temperature, the precipitate was collected by centrifugation and washed repeatedly with deionized water and ethanol to remove impurities. The product was then dried overnight in a vacuum oven at 40 $^oC$. Meso-(CuFe)O nanosheets were finally obtained by directly calcining dried powder under air at 300 $^oC$ for 3 h. Similarly, meso-(CeFe)O nanosheets with different Fe amounts were prepared with different added ratios of $Fe(NO_3)_3{\cdot}9H_2O$ and $Cu(NO_3)_2{\cdot}3H_2O$, while meso-CuO was synthesized by the same procedure but with $Cu(NO_3)_2{\cdot}3H_2O$ as the sole metal precursor.

**Electrocatalytic measurement**

All electrochemical measurements were performed on a CHI 660E electrochemical workstation (Chenhua, Shanghai) at 25 °C in a single-cell separated by a proton-exchange membrane (Nafion 117). A standard three-electrode configuration was used, with Ag/AgCl (saturated KCl) as the reference electrode and a carbon rod as the counter electrode. All potentials were measured versus Ag/AgCl and converted to the RHE according to $E_{RHE}=E_{Ag/AgCl}$ + (0.197 + 0.0591 × pH). LSV curves were first performed from 1.5 to 3.0 V at a scan rate of 10.0 mV $s^{-1}$ until the steady-state polarization curves were obtained. EIS spectra were then conducted over a frequency range of 100 kHz to 0.1 Hz with an AC amplitude of 5.0 mV. FE and formamide yields were determined at a series of constant applied potentials by the chronoamperometry. Unless otherwise stated,

potentiostatic electrocatalysis was carried out in 20 mL of electrolyte a single-cell setup for 1 h. All potentials were reported versus RHE unless otherwise specified.

**Product Analysis**

Liquid products were analyzed by the nuclear magnetic resonance (NMR) spectrometer. $^{1}$H NMR and $^{13}$C NMR spectra were recorded on a Bruker AVANCE 400 spectrometer operating at 400 MHz. For $^{1}$H NMR and $^{13}$C NMR analysis, unless otherwise stated, 500 μL of electrolyte was added 100 μL of $D_2O$ with maleic acid (MA) at a concentration of 4.0 mg mL$^{-1}$ as an internal standard.

**Determination of nitrate:** Firstly, a certain amount of electrolyte was taken out from the electrolytic cell and diluted to 5 mL to detection range. Then, 0.1 mL 1 M HCl and 0.01 mL 0.8 wt% sulfamic acid solution were added into the aforementioned solution. The absorption spectrum was measured using an ultraviolet-visible spectrophotometer and the absorption intensities at a wavelength of 220 nm and 275 nm were recorded after sitting for 20 min. The final absorbance value was calculated by this equation: $A=A_{220nm}-2A_{275nm}$.

**Determination of nitrite:** A mixture of p-aminobenzenesulfonamide (4 g), N-(1-naphthyl) ethylenediamine dihydrochloride (0.20 g), ultrapure water (50 mL), and phosphoric acid (10 mL, ρ=1.70 g/mL) was used as a color reagent. A certain amount of electrolyte was taken out from the electrolytic cell and diluted to 5 mL to detection range. Next, 0.1 mL color reagent was added into the aforementioned 5 mL solution and mixed uniformity, and the absorption intensity was recorded after sitting for 20 min. The final absorbance value was absorption intensities at 540 nm.

Yield rate (mmol h$^{-1}$ cm$^{-1}$) of formamide and formate was calculated using the following equation:

$$Yield\ rate = \frac{2N_{product}}{t}$$

Faraday efficiency (FE, %) of product was determined by the following equation:

$$FE\ (\%) = \frac{N_{product} \times n \times F}{Q} = \frac{N_{product} \times n \times F}{\int_0^t I\ dt}$$

Selectivity (%) of product was determined by the following equation:

$$Selectivity(\%) = \frac{C_{product} \times N_{Product}}{C_{consumed\ substrate} \times N_{consumed\ substrate}}$$

where *N* is the amount of substance; *t* is the electrocatalytic time; *F* is the Faraday constant (96485 C mol$^{-1}$), *n* is the number of transferred electrons; *Q* is obtained from the integral of i-*t* curve and is the total charge passed through the electrode; *C* is the number of carbon atoms contained in a molecule of product or substrate.

**References**


1. Li, J., Zhang, Y., Kuruvinashetti, K. & Kornienko, N. Construction of C–N bonds from small-molecule precursors through heterogeneous electrocatalysis. *Nat. Rev. Chem.* **6**, 303-319 (2022).
2. Wu, Y., Liu, X., Huang, Y., Meng, N. & Zhang, B. Electrocatalytic C–N bond construction from inorganic nitrogen sources in water. *Nat. Protoc.* **21**, 3098-3126 (2026).
3. Wang, X. et al. Revisiting Pt foil catalysts for formamide electrosynthesis achieved at industrial-level current densities. *Nat. Commun.* **16**, 8040 (2025).
4. Beyazay, T., Martin, W. F. & Tüysüz, H. Direct Synthesis of Formamide from $CO_2$ and $H_2O$ with Nickel–Iron Nitride Heterostructures under Mild Hydrothermal Conditions. *J. Am. Chem. Soc.* **145**, 19768-19779 (2023).
5. Fan, Y. et al. Electrochemical synthesis of formamide by C–N coupling with amine and $CO_2$ with a high faradaic efficiency of 37.5%. *Chem* **10**, 2437-2449 (2024).
6. Jiao, Y. et al. Photoelectrocatalytic Upgrading of Biomass Derivatives for Efficient C–N Coupling with Formamide. *J. Am. Chem. Soc.* **147**, 31679-31688 (2025).
7. Li, R. et al. Strong dipole-promoted N–O bond hydrogenolysis enables ampere-level electrosynthesis of methylamine. *Nat. Chem.* **17**, 1152-1160 (2025).
8. Liu, C., Gao, Y. & Zhang, B. Organonitrogen electrosynthesis from $CO_2$ and nitrogenous sources in water. *Nat. Synth.* **3**, 794-796 (2024).
9. Pan, Y. et al. Reversing the reduction sequence of aldehydes and nitriles for electrochemical C–N coupling. *Nat. Synth.* **5**, 1231-1241 (2026).
10. Wu, Y., Jiang, Z., Lin, Z., Liang, Y. & Wang, H. Direct electrosynthesis of methylamine from carbon dioxide and nitrate. *Nat. Sustain.* **4**, 725-730 (2021).
11. Peng, C. et al. Homo/Heterogeneous Dual Active Centers Enable Selective Electrochemical C–N Coupling of $CO_2$ and Nitrate to Formamide. *Angew. Chem. Int. Ed.* **65**, e9113894 (2026).
12. McKee, M. et al. Electrochemical C–N Bond Formation from $CO_2$ and Nitrate Using Molecular Catalysis. *J. Am. Chem. Soc.* **148**, 39535-39545 (2026).
13. Lan, J. et al. Efficient electrosynthesis of formamide from carbon monoxide and nitrite on a Ru-dispersed Cu nanocluster catalyst. *Nat. Commun.* **14**, 2870 (2023).
14. Li, J. et al. Heterogeneous electrosynthesis of C–N, C–S and C–P products using $CO_2$ as a building block. *Nat. Synth.* **3**, 809-824 (2024).
15. Guo, C. et al. Coupled electrosynthesis of formamide with ~100% carbon and nitrogen selectivity via matching cathode–anode local pH. *Nat. Commun.* **17**, 9317 (2026).
16. Sun, Y. et al. Ordered heteronuclear metal pairs facilitate urea electrosynthesis. *Nat. Synth.* 2026).
17. Shen, B. et al. Local Acidic Microenvironments Enhanced Anodic Formamide Electrosynthesis over Isolated Pd Sites. *Angew. Chem. Int. Ed.* **65**, e21334 (2026).
18. Meng, N. et al. Electrosynthesis of formamide from methanol and ammonia under ambient conditions. *Nat. Commun.* **13**, 5452 (2022).
19. Wang, H. et al. Dual Redox Shuttles Drive Efficient Formamide Electrosynthesis. *J. Am. Chem. Soc.* **148**, 8464-8473 (2026).
20. Shi, Q. et al. Electrocatalytic Upgrading of Plastic and Biomass-Derived Polyols to Formamide under Ambient Conditions. *Angew. Chem. Int. Ed.* **63**, e202407580 (2024).
21. Liu, Z. et al. Directing the Electrochemical C–N Coupling Toward Efficient Amide Synthesis via Ammonia Activation-Mediated Pathway. *Angew. Chem. Int. Ed.* **64**, e202518108 (2025).
22. Lee, E. Y. & Sarwar, A. Methanol-tolerant yeast for biofuel production. *Nat. Metab.* **4**, 800-801 (2022).
23. Verma, S., Lu, S. & Kenis, P. J. A. Co-electrolysis of $CO_2$ and glycerol as a pathway to carbon chemicals with improved technoeconomics due to low electricity consumption. *Nat. Energy* **4**, 466-474 (2019).
24. Han, S. & Liu, B. Robust Formate Electrosynthesis from Mixed Biomass Polyols by a Direct Carbon–Carbon Bond Cleavage Route. *J. Am. Chem. Soc.* **148**, 778-789 (2025).
25. Huber, G. W., Iborra, S. & Corma, A. Synthesis of Transportation Fuels from Biomass: Chemistry, Catalysts,

and Engineering. *Chem. Rev.* **106**, 4044−4098 (2006).
26. Han, S., Ding, R., Tang, D. & Liu, B. Electrocatalytic C–S Coupling for Efficient Organosulfur Electrosynthesis from Mixed Polyols with >99% of Carbon Selectivity. *J. Am. Chem. Soc.* **148**, 13404-13413 (2026).
27. Xu, X. et al. Unraveling the Crystal-Field-Mediated Cobalt Spin-State Evolution for Electrocatalytic Ethylene Glycol Oxidation by In Situ X-Ray Emission Spectroscopy. *Angew. Chem. Int. Ed.* **65**, e4512481 (2026).
28. Xia, Q. et al. Electrochemical Upgrading Plastic to Organosulfurs Through Fe-$N_3$ Single Atom Catalyst Under Ambient Conditions. *Angew. Chem. Int. Ed.* **64**, e202507901 (2025).
29. Ya, Z. et al. Electro- and Photocatalytic C–X Bond Coupling in Valorization of Waste Plastics/Biomass: Reaction Mechanism and Catalyst Engineering. *Adv. Mater.* **38**, e74524 (2026).
30. Xia, Q. et al. Efficient synthesis of organosulfur compounds via electrochemical biomass conversion. *Nat. Synth.* **4**, 765-775 (2025).
31. Zhang, Y. et al. Oxy-reductive C-N bond formation via pulsed electrolysis. *Nat. Commun.* **16**, 8106 (2025).
32. Roithmeyer, H. et al. Electrocatalytic Ammonia Oxidation with a Tailored Molecular Catalyst Heterogenized via Surface Host–Guest Complexation. *J. Am. Chem. Soc.* **146**, 430-436 (2023).
33. Liu, H.-Y., Lant, H. M. C., Decavoli, C., Crabtree, R. H. & Brudvig, G. W. pH-Dependent Electrocatalytic Aqueous Ammonia Oxidation to Nitrite and Nitrate by a Copper(II) Complex with an Oxidation-Resistant Ligand. *J. Am. Chem. Soc.* **147**, 1624-1630 (2025).
34. Wang, T. et al. Combined anodic and cathodic hydrogen production from aldehyde oxidation and hydrogen evolution reaction. *Nat. Catal.* **5**, 66-73 (2021).
35. Pi, M. et al. Observation of Robust Compressed $CuO_6$ Octahedra and Exotic Spin Structure in $CaCuFe_2O_5$. *J. Am. Chem. Soc.* **147**, 4403-4410 (2025).
36. Greiner, M. T., Jones, T. E., Klyushin, A., Knop-Gericke, A. & Schlögl, R. Ethylene Epoxidation at the Phase Transition of Copper Oxides. *J. Am. Chem. Soc.* **139**, 11825-11832 (2017).
37. Zhu, S. et al. Cooperative spin alignment enhances dimerization in the electrochemical ammonia oxidation reaction. *Nat. Chem.* **18**, 258-265 (2025).
38. Wang, Q. et al. Highly Crystalline and Porous Borocarbonitrides as Metal-Free Catalysts for Boosted N-Heterocycle Dehydrogenation. *Angew. Chem. Int. Ed.* **65**, e5627455 (2026).
39. Hu, M. et al. Template-free Synthesis of Mesoporous and Crystalline Transition Metal Oxide Nanoplates with Abundant Surface Defects. *Matter* **2**, 1244-1259 (2020).
40. Fu, L. et al. Electrodeposition-initiated, self-catalyzed growth of 2D amorphous Fe-group metal–boron alloy mesoporous films. *Nat. Commun.* **17**, 9325 (2026).
41. Hao, L. L. et al. Engineering d–d Coupling-Induced Ferromagnetic Catalysts for Boosting the Spin-Polarized Water Oxidation. *J. Am. Chem. Soc.* **148**, 10522-10531 (2026).
42. Xie, F., Du, Y., Lu, M., Yan, S. & Zou, Z. Thermal-stimulated spin disordering accelerates water electrolysis. *Energy Environ. Sci.* **18**, 1972-1983 (2025).
43. Ge, Y. et al. Charge-Spin-Orbit Modulated Carbon-Encapsulated FeP/$Fe_3O_4$ Heterojunctions for Ultrafast and Stable Conversion of Low-Concentration Nitrate to Ammonia. *Angew. Chem. Int. Ed.* **65**, e19571 (2025).
44. Kurebayashi, H. et al. Dynamical stability by spin transfer in nearly isotropic magnets. *Nat. Mater.* **25**, 1167-1174 (2026).
45. Li, Y., Che, Y., Lv, H., Wu, X. & Yang, J. Noninnocent Ligands as a Design Strategy for Fully Compensated Ferrimagnetism in Two-Dimensional Metal–Organic Frameworks. *J. Am. Chem. Soc.* **148**, 32033-32040 (2026).
46. Li, X. et al. Electron transfer in catalysis: from fundamentals to strategies. *Chem. Soc. Rev.* **54**, 11423-11467 (2025).
47. Wang, S. et al. Nanoscale high-entropy surface engineering promotes selective glycerol electro-oxidation to glycerate at high current density. *Nat. Nanotech.* **20**, 646-655 (2025).
48. Li, Y. et al. PtAu alloying-modulated hydroxyl and substrate adsorption for glycerol electrooxidation to $C_3$ products. *Energy Environ. Sci.* **17**, 4205-4215 (2024).
49. Lan, J. et al. Atomically ordered dual atomic pairs in $CuAuZn_2$ intermetallics for efficient urea

electrosynthesis. *Nat. Synth.* 2026).
50. Guo, C. et al. Electrochemical Upgrading of Formic Acid to Formamide via Coupling Nitrite Co-Reduction. *J. Am. Chem. Soc.* **144**, 16006-16011 (2022).
51. Sun, L., Jing, Y. & Liu, B. Electrochemical and chemical cascade catalysis for efficient hexamethylenetetramine synthesis over mesoporous copper nanotips. *Nat. Commun.* **17**, 6664 (2026).
52. Zhang, Y. et al. Modulating p-d Orbital Hybridization in Mesoporous Medium-Entropy Alloy Nanozymes with Enhanced Peroxidase-Like Activity. *ACS Nano* **19**, 24013-24022 (2025).
53. Wang, L. et al. A polymer tethering strategy to achieve high metal loading on catalysts for Fenton reactions. *Nat. Commun.* **14**, 7841 (2023).
54. He, H. et al. High-Entropy Effect of Mesoporous Metal Oxides Promotes Tandem Catalysis for Efficient Ammonia Electrosynthesis from Nitrate. *Adv. Mater.* **37**, e08982 (2025).
55. Zhang, Q. et al. Active Hydroxyl-Mediated Preferential Cleavage of Carbon-Carbon Bonds in Electrocatalytic Glycerol Oxidation. *Angew. Chem. Int. Ed.* **64**, e202420942 (2025).
56. Wu, L. et al. Strengthening the Synergy between Oxygen Vacancies in Electrocatalysts for Efficient Glycerol Electrooxidation. *Adv. Mater.* **36**, 2401857 (2024).
57. Wang, H. et al. Electrochemical coupling of $CO_2$ and phosphite for foscarnet synthesis. *Nat. Catal.* **9**, 989-997 (2026).

**Acknowledgements**

This work was financially supported by the National Key Research and Development Program of China (2023YFC3905002), the National Natural Science Foundation of China (22575159), and the Fundamental Research Funds for the Central Universities. The authors would like to thank Dr. Feng Yang (the Comprehensive Training Platform of the Specialized Laboratory, College of Chemistry, Sichuan University) for her assistance with TEM/STEM imaging and Dr. Yanping Huang (the Center of Engineering Experimental Teaching, School of Chemical Engineering, Sichuan University) for her help of SEM imaging.

**Contributions**

B.L. conceived the project and designed the experiments. S.H. performed the catalysts preparation and characterizations, the performance evaluation, and the mechanism exploration. D.T. conducted the DFT calculations and assisted the mechanism study. R.D. helped the performance evaluation. All the authors discussed the results, analyzed the data, and cowrote the paper.

**Completing Interests**

The authors declare no completing interest.

**Supplementary Information**

Supporting Experiments, including materials synthesis and characterizations, more electrocatalytic tests and mechanism analysis, **Fig. S1-S24 and Tables S1-S5**.

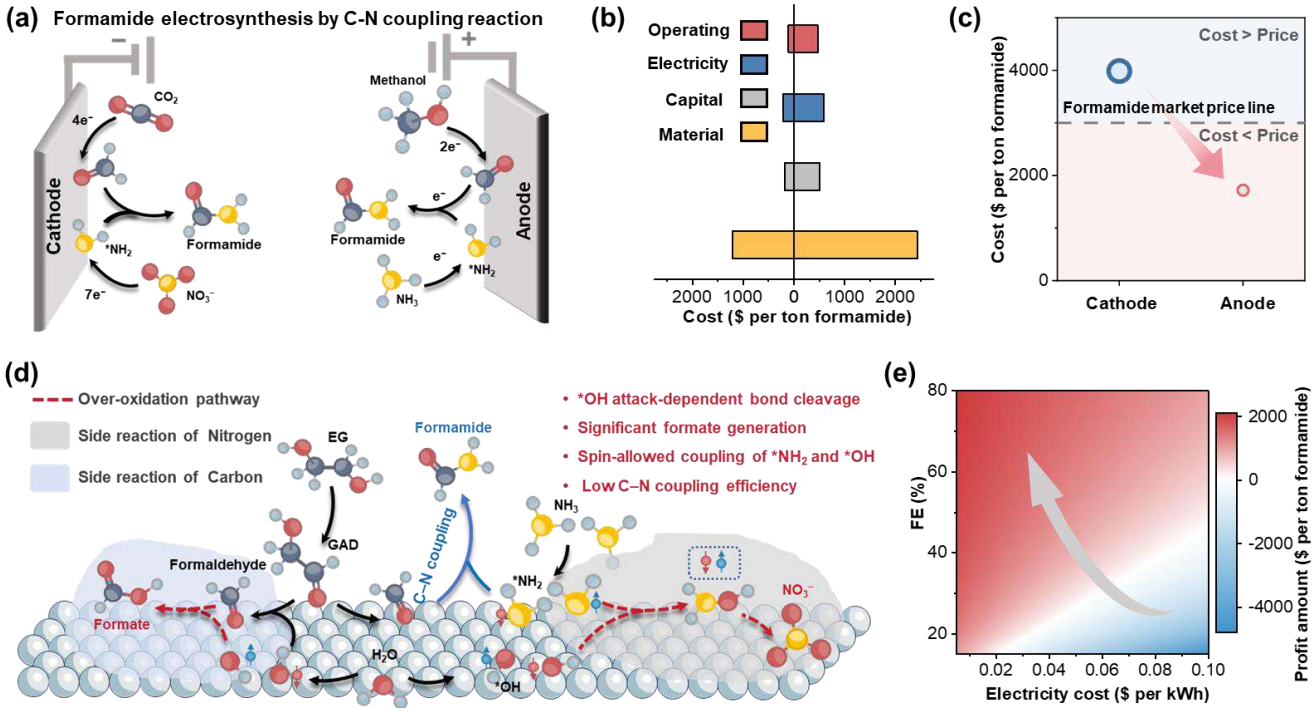



**Fig. 1. Economic comparison of electrocatalytic formamide synthesis via C–N coupling reactions at the cathode and anode.** (**a**) Schematic illustration of formamide electrosynthesis at the cathode and anode, showing different electron transfer pathways. (**b**) Cost breakdown (operation, electricity, capital, material) and (**c**) total cost per ton of formamide by electrocatalytic cathodic and anodic routes. (**d**) Mechanistic diagram highlighting the traditional *OH-mediated C–C cleavage routes with main side reactions of nitrogen and carbon. (**e**) Heatmap of FE and profit as a function of electricity cost for the anodic route, indicating the economic feasibility.

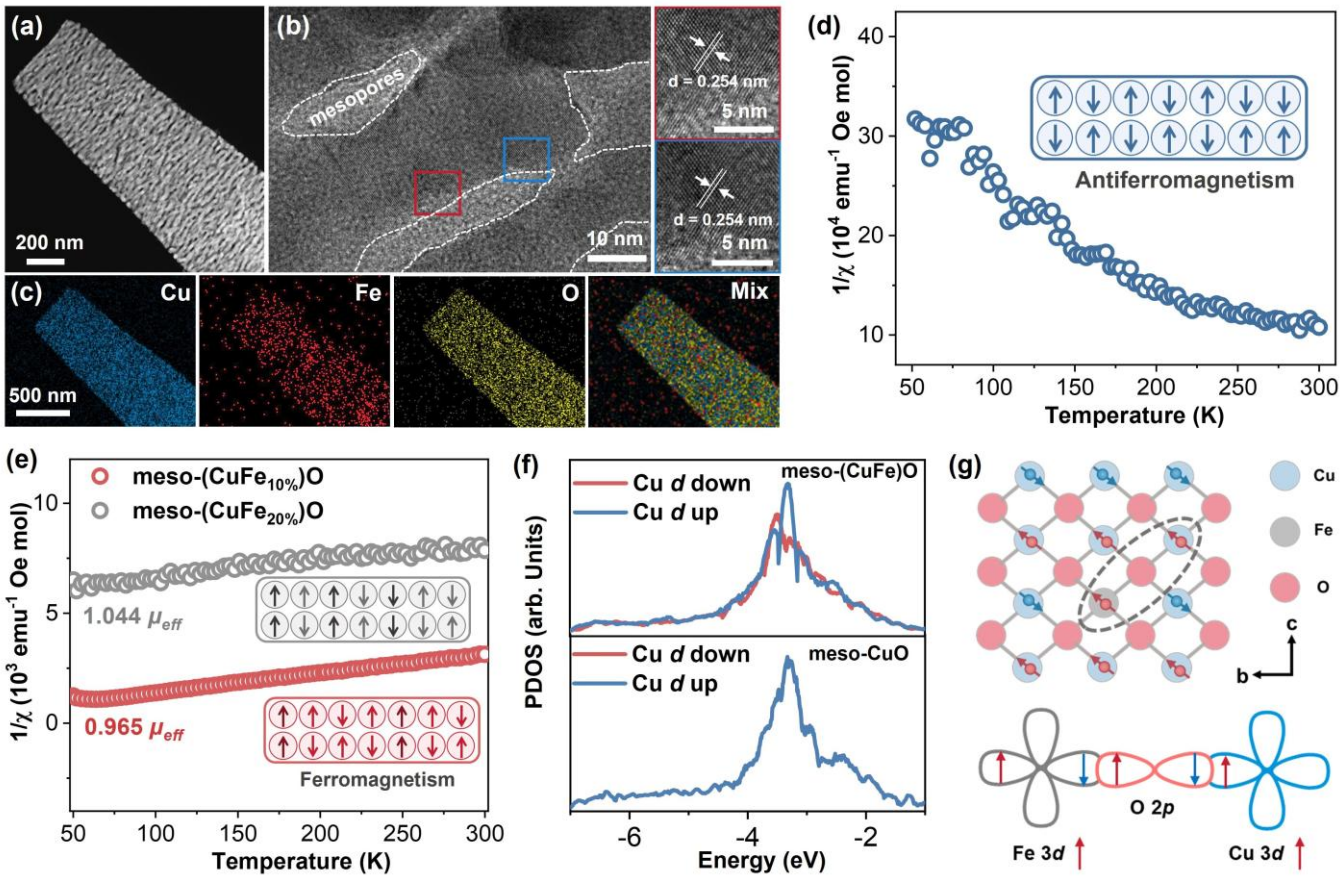



**Fig. 2. Structural and magnetic characterizations of spin-polarized meso-(CuFe)O.** (**a**) HAADF-STEM image showing the nanosheet morphology. (**b**) High-magnification and high-resolution TEM images displaying penetrated mesopores and lattice fringes. (**c**) EDS elemental mapping images of Cu, Fe, O, and their overlay, indicating bimetallic compositions. (**d**) Temperature-dependent inverse magnetic susceptibility (1/χ) of meso-CuO, showing antiferromagnetic behavior. (**e**) 1/χ versus temperature for meso-($CuFe_{10\%}$)O and meso-($CuFe_{20\%}$)O, with fitted effective magnetic moments. (**f**) Projected density of states (PDOS) of Cu *d* orbitals (up and down spins) for meso-(CuFe)O and meso-CuO. (**g**) Schematic illustration of the spin configurations in meso-(CuFe)O.

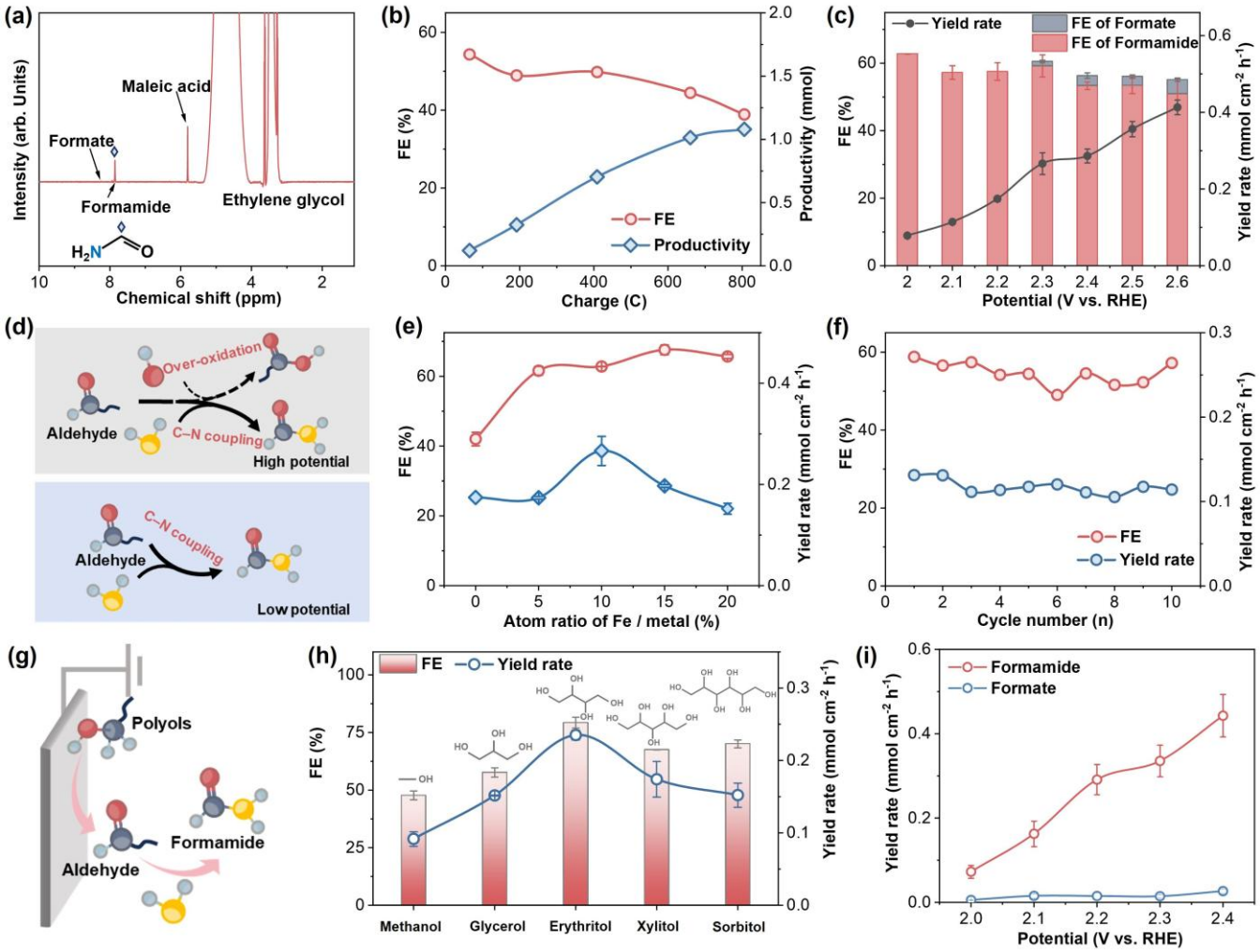



**Fig. 3. Electrocatalytic performance of spin-polarized meso-(CuFe)O for sustainable formamide synthesis at anode.** (**a**) $^{1}$H NMR spectrum of the electrolyte for formamide synthesis after electrocatalysis at 2.5 V. (**b**) FE and productivity of formamide as a function of charges. (**c**) FE and yield rates of formamide collected at different test potentials. (**d**) Schematic illustration of the potential-dependent reaction pathways. (**e**) FE and yield rates of formamide with different Fe contents in spin-polarized meso-(CuFe)O. (**f**) FE and yield rates during stability tests for 10 cycles. (**g**) Schematic illustration of formamide synthesis with different polyols as the substrates. (**h**) FE and yield rates of formamide using different polyols as the substrates tested at 2.2 V. (**i**) Yield rates of formamide and formate collected in a mixed polyol system at different potentials.

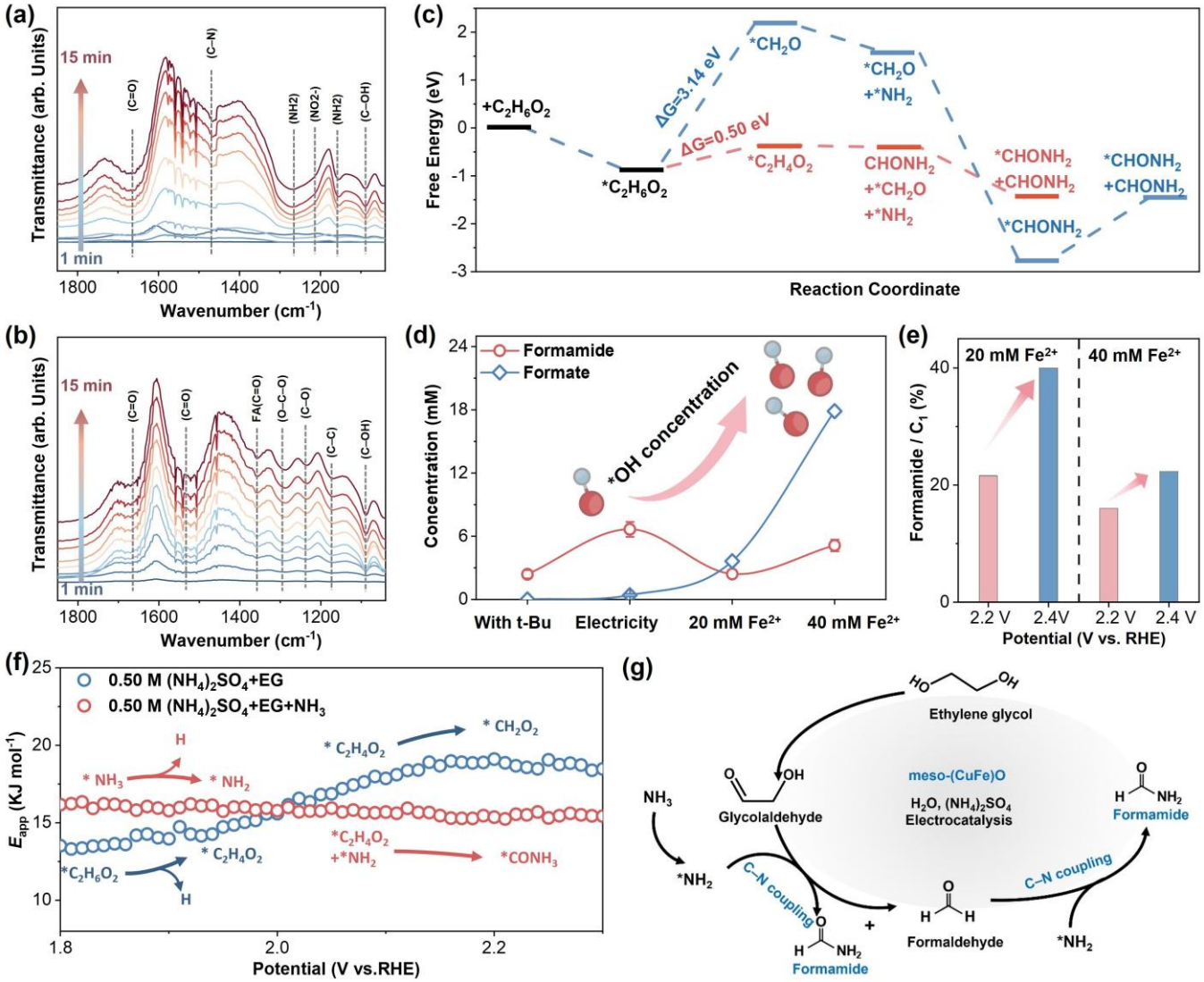



**Fig. 4. Electrocatalytic pathway of spin-polarized meso-(CuFe)O for anodic formamide synthesis.** (**a**) *In situ* FTIR spectra of the electrolyte containing only ethylene glycol and (**b**) containing ethylene glycol and $NH_3$ during electrocatalysis at 2.2 V. (**c**) DFT-calculated free energy profiles for the reaction pathways with and without $NH_3$ participation. (**d**) Concentrations of formamide and formate after electrocatalysis with tert-butanol addition or with different $Fe^{2+}$ concentrations (20 and 40 mM with 300 mM and 600 mM $H_2O_2$, respectively) to introduce additional *OH. (**e**) Formamide selectivity in $C_1$ products at 2.2 and 2.4 V with 20 and 40 mM $Fe^{2+}$. (**f**) Apparent activation energy ($E_{app}$) as a function of potentials for the electrolyte with ethylene glycol only and with ethylene glycol and $NH_3$. (**g**) Schematic illustration of proposed *$NH_2$-mediated ethylene glycol oxidation and C–N coupling pathway over spin-polarized meso-(CuFe)O.

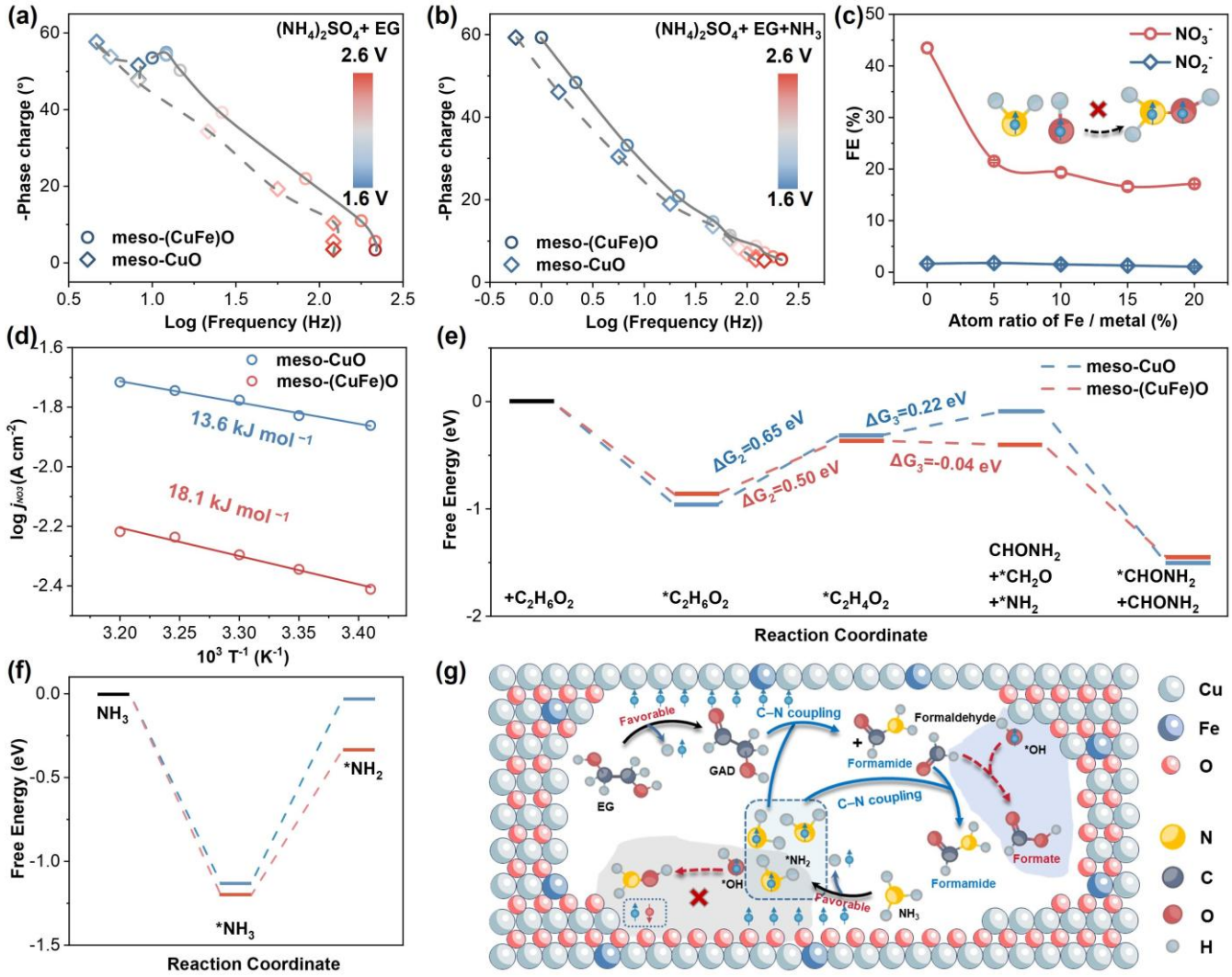



**Fig. 5. Spin-polarization-mediated mechanism of meso-(CuFe)O for anodic formamide electrosynthesis.** (**a**) Bode phase plots of meso-(CuFe)O and meso-CuO collected in $(NH_4)_2SO_4$ + ethylene glycol and (**b**) in $(NH_4)_2SO_4$ + ethylene glycol + $NH_3$. (**c**) FE of $NO_3^-$ and $NO_2^-$ as a function of Fe contents at 2.1 V. (**d**) Arrhenius plots for $NH_3$ overoxidation to $NO_3^-$ on meso-CuO and meso-(CuFe)O. (**e**) DFT-calculated free energy profiles for $NH_3$ dehydrogenation to $*NH_2$. (**f**) DFT-calculated free energy profiles for ethylene glycol oxidation and C–N coupling on meso-CuO and meso-(CuFe)O. (**g**) Schematic illustration of the spin-polarization-mediated mechanism for anodic formamide synthesis.

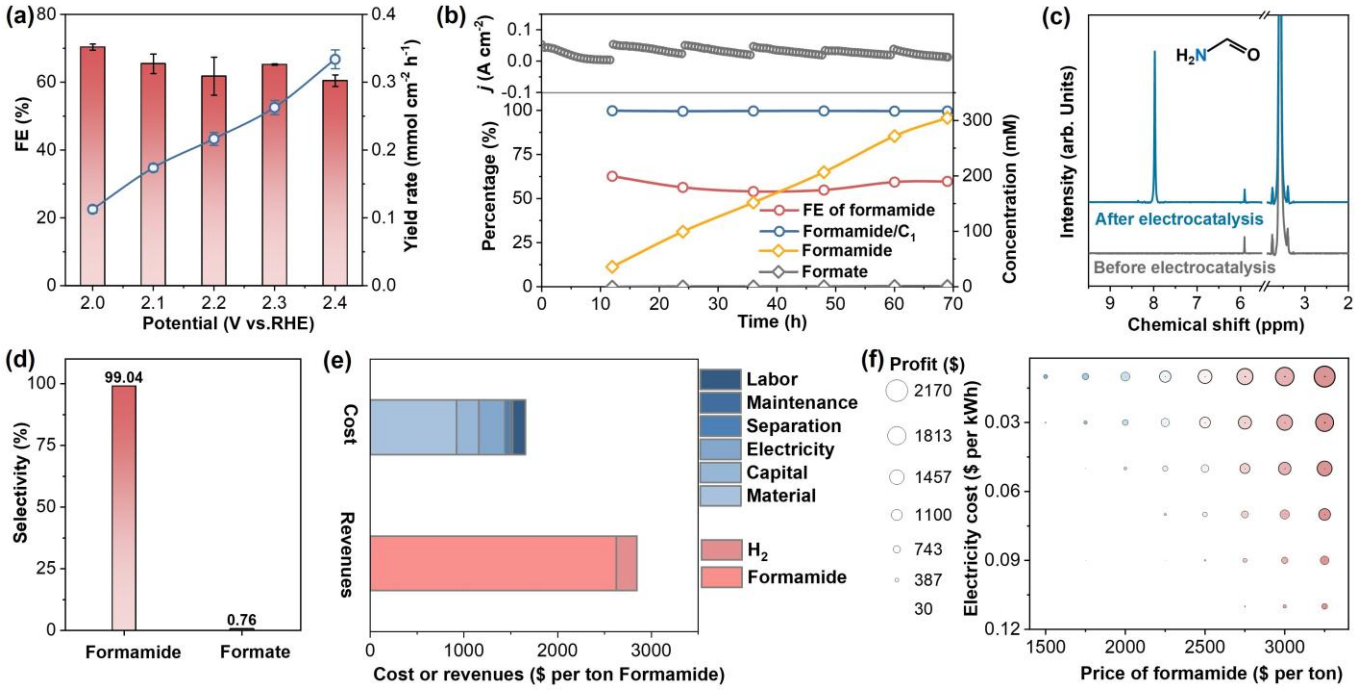



**Fig. 6. Flow-cell performance and techno-economic analysis of anodic formamide electrosynthesis.** (**a**) FE and yield rates of formamide collected at different potentials. (**b**) Long-term stability test at 2.2 V, showing current density, FE of formamide, formamide/$C_1$ ratio, formamide concentration, and formate concentration over 20 h. (**c**) $^1$H NMR spectra of the electrolyte before and after electrocatalysis. (**d**) Selectivity of formamide and formate after deep conversion of ethylene glycol. (**e**) Cost and revenue breakdown per ton of formamide. (**f**) Profit analysis as a function of electricity cost and formamide price.

## Supplementary Files

This is a list of supplementary files associated with this preprint. Click to download.

- HanCNSI.docx